ACS central science

Research Article

Cite This: ACS Cent. Sci. 2018, 4, 1412−1419

http://pubs.acs.org/journal/acscii

Multimetallic Hollow Mesoporous Nanospheres with Synergistically Structural and Compositional Effects for Highly Efficient Ethanol Electrooxidation

Hao Lv,[†] Aaron Lopes,[‡] Dongdong Xu,*[,†] and Ben Liu*[,†]

[†]Jiangsu Key Laboratory of New Power Batteries, Jiangsu Collaborative Innovation Center of Biomedical Functional Materials, School of Chemistry and Materials Science, Nanjing Normal University, Nanjing 210023, China

[‡]Department of Chemical Engineering, Massachusetts Institute of Technology, Cambridge, Massachusetts 02139, United States

Supporting Information

ABSTRACT: Controlling the nanostructures and chemical compositions of the electrochemical nanocatalysts has been recognized as two prominent means to kinetically promote the electrocatalytic performance. Herein, we report a general "dual"-template synthesis methodology for the formation of multimetallic hollow mesoporous nanospheres (HMSs) with an adjustable interior hollow cavity and cylindrically opened mesoporous shell as a highly efficient electrocatalyst for ethanol oxidation reaction. Three-dimensional trimetallic PdAgCu HMSs were synthesized via in situ coreduction of Pd, Ag, and Cu precursors on "dual"-template structural directing surfactant of dioctadecyldimethylammonium chloride in optimal synthesis conditions. Due to synergistic advantages on hollow mesoporous nanostructures and multimetallic compositions, the resultant PdAgCu HMSs exhibited significantly enhanced electrocatalytic performance toward ethanol oxidation reaction with a mass activity of 5.13 A mg_{Pd}^{-1} at a scan rate of 50 mV s^{-1} and operation stability (retained 1.09 A mg_{pd}^{-1} after the electrocatalysis). The "dual"-template route will open a new avenue to rationally design multimetallic HMSs with controlled functions for broad applications.

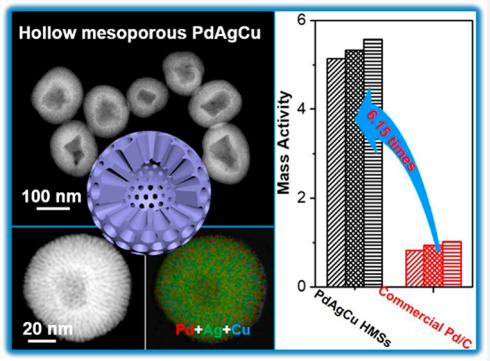

INTRODUCTION

The rational design and synthesis of noble metal nanocrystals with controlled nanostructures and functions have received enormous attention due to their broad applications in (electro)-catalysis, sensors, bioimaging, drug delivery, and so forth.[1−4] Among the various nanostructures of noble metal nanocrystals, hierarchically hollow mesoporous nanospheres (HMSs) with an interior hollow cavity and mesoporous shell have recently been of high interest.[5−7] Three-dimensional (3D) HMSs not only decrease the mass density of noble metals, but also enlarge the surface area to expose more accessible active sites. Specifically, the mesoporous shell with shortened and opened nanochannels of the HMSs would further facilitate mass transfer during the catalysis kinetically.[8,9] These merits endow the HMSs with excellent (electro)catalytic performance. A number of synthetic methods and techniques have been developed to prepare nanosized HMSs, including the surfactant route,[10−14] emulsion approach,[15,16] and hard-template route.[17−21] Unfortunately, successful synthesis of the HMSs mostly focuses on silica, carbon, and metal compounds.[5,6,22] Noble metal nanocrystals-based HMSs are rarely reported, especially by surfactant-directed synthesis,[23,24] possibly because of the complexity and difficulty in tuning the crystalline nucleation kinetics of noble metal precursors while simultaneously maintaining the assembled hollow mesoporous structures during the synthesis.

The introduction of less-expensive secondary metals into noble metal nanocrystals to form multimetallic nanoalloys also enhances their catalytic performance and meanwhile enlarges the utilization efficiency of noble metals.[25−30] Taking electrocatalytic ethanol oxidation reaction (EOR) as the example, alloying Pd with more oxophilic metals (e.g., Au, Ag, Ru, Cu, or Ni) would facilitate the formation of surface-adsorbed OH (OH_{ads}). This promotes the direct oxidation reaction of OH_{ads} with poisoning intermediates, and eventually accelerates EOR.[31,32] Besides, the adsorption affinity strength of poisoning intermediates on Pd-based alloyed nanocatalysts would also be weakened through the d-band theory, and also enhance mass activity in EOR accordingly.[33,34] Recently, some researchers found that, when alloying the third (and even fourth) metals into multimetallic nanoalloys, the catalytic performance was further enhanced due to the synergistic composition effects compared to their bimetallic counterparts.[35−37] On the basis of above discussions, therefore, a high-performance nanocatalyst can be expected when combining synergistically structural and compositional effects, including hollow mesoporous shell and multimetallic nanoalloy. However, the surfactant-directed formation of multimetallic Pd-based hollow mesoporous

Received: July 24, 2018
Published: September 18, 2018

DOI: 10.1021/acscentsci.8b00490
ACS Cent. Sci. 2018, 4, 1412−1419

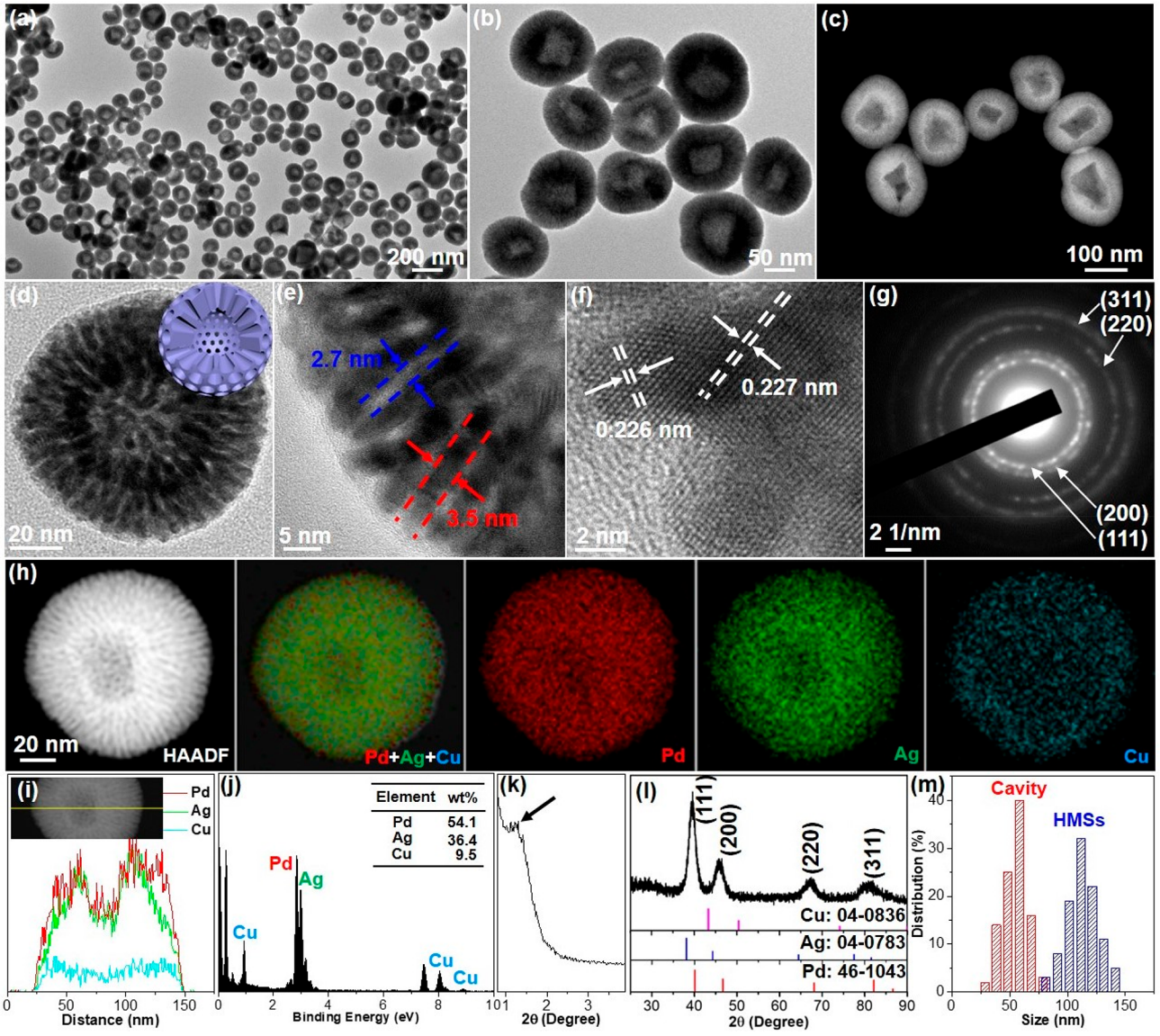

Figure 1. Structural characterizations. (a, b) Low-magnification TEM and (c) HAADF-STEM images of trimetallic PdAgCu HMSs. (d, e) High-magnification, (f) high-resolution TEM images, and (g) SAED pattern of PdAgCu HMSs. Inset in (d) is the scheme of a HMS. (h) HAADF-STEM mappings and (i) line scan analysis of Pd, Ag, and Cu in trimetallic PdAgCu HMSs. (j) STEM-EDX, (k) small-angle, and (l) wide-angle XRD patterns of PdAgCu HMSs. (m) Size distributions of interior hollow cavity and whole nanospheres in PdAgCu HMSs.

nanostructures is highly challenging and has not yet been achieved thus far.

Herein, we presented a facile yet effective aqueous synthesis of trimetallic PdAgCu HMSs with an adjustable interior hollow cavity and mesoporous shell through a simple, one-pot "dual" micelle template route for the first time. The introduction of dioctadecyldimethylammonium chloride (DODAC) as the "dual"-template structural directing surfactant and using Ag as the cometal under the optimal synthesis conditions were found to be critical for the formation of multimetallic Pd-based HMSs. The resultant PdAgCu HMSs combined multiple merits, including multimetallic composition, and a hollow and mesoporous nanostructure with cylindrically opened nanochannels, and thus synergistically boosted the electrocatalytic performance toward electrochemical EOR. The origin of enhanced electrocatalytic performance was also kinetically elucidated by CO antipoisoning experiments, in comparison to bimetallic and solid mesoporous counterpart catalysts.

RESULTS AND DISCUSSION

The morphology and nanostructure of as-made trimetallic PdAgCu HMSs, which were synthesized with the surfactant of DODAC, metal coprecursors of H_2PdCl_4, $AgNO_3$, and $Cu(NO_3)_2$, and reducing agent of ascorbic acid (see experimental for more synthesis details),[38−40] were carefully characterized by transition electron microscopy (TEM) and high-angle annular dark-field scanning TEM (HAADF-STEM). As shown in Figure 1a,b, the typical low-magnification TEM images exhibited monodispersed and uniform hollow structured nanospheres with a well-defined mesoporous shell. The diameter of HMSs was in the range of 85−140 nm with an average interior hollow cavity size of 55 nm and mesoporous shell thickness of 30 nm (Figure 1m). Uniform mesoporous nanostructures with a pretty clear interior hollow cavity were further indicated by HAADF-STEM (Figure 1c, see more TEM and STEM images in Figure S1). The high-magnification TEM image of an individual HMS was provided to further distinguish interior hollow cavity and

DOI: 10.1021/acscentsci.8b00490
ACS Cent. Sci. 2018, 4, 1412−1419

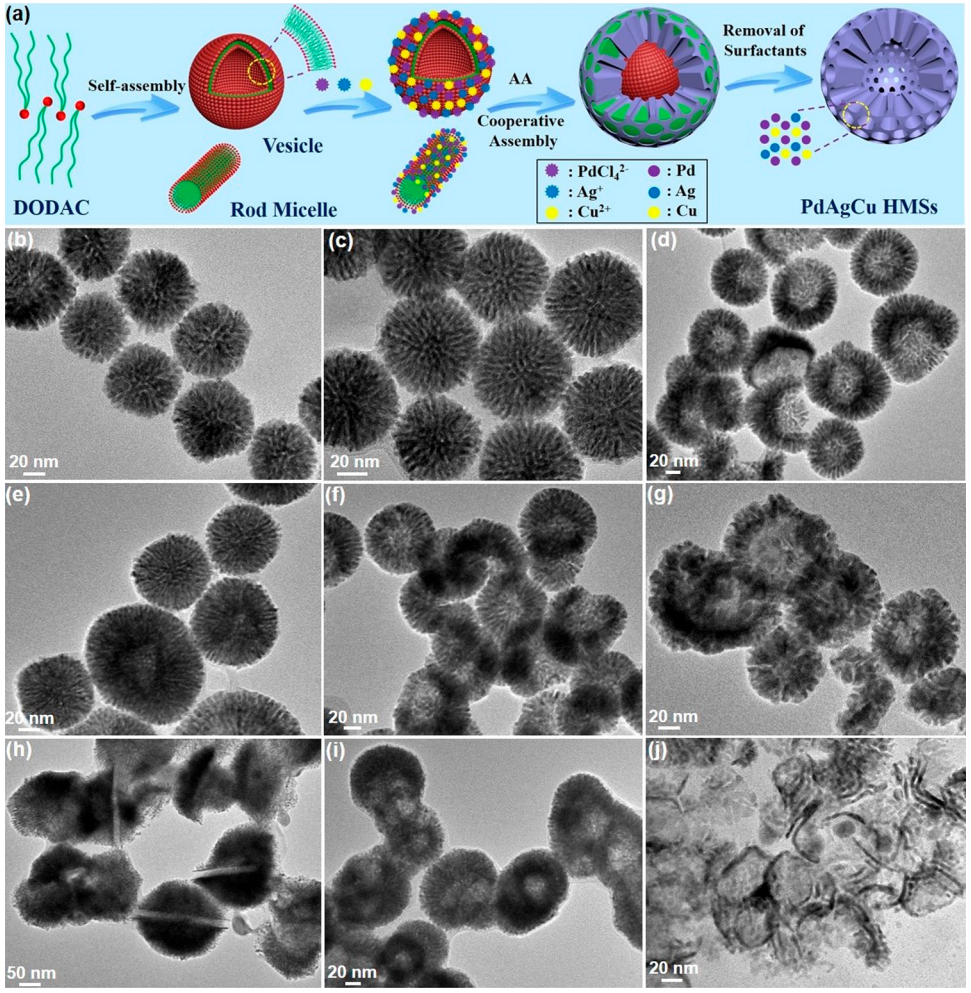

Figure 2. Formation mechanism. (a) Schematic illustrating the formation of trimetallic PdAgCu HMSs based on a "dual"-template route. TEM images of (b) monometallic Pd MSs, (c) bimetallic PdCu MSs and (d) bimetallic PdAg HMSs. TEM images of trimetallic PdAgCu nanostructures synthesized with (e–g) different Ag contents and (h–j) pH values.

mesoporous shell. As shown in Figure 1d, the hollow nanosphere composed of the nearly defect-free mesopores in the whole shell. Mesoporous nanochannels were ordered and cylindrically opened (as schematically marked in Figure 1d). The average mesopore size was 2.7 nm with a wall thickness of 3.5 nm (Figure 1e). Mesoporous framework of HMSs was also revealed by small-angle X-ray diffraction (XRD) (Figure 1k). A typical diffraction peak appeared at 1.3°, indicating that the cell parameter of the mesoporous shell was 6.8 nm, in line with the results observed from TEM (6.2 nm).

The crystallinity and trimetallic chemical compositions of PdAgCu HMSs were further revealed. A face-centered cubic (fcc) lattice fringe was clearly observed from the high-resolution TEM image, as indicated by PdAgCu (111) plane with a *d*-spacing of 0.226 nm (Figure 1f). The selected-area electron diffraction (SAED) (Figure 1g) and wide-angle XRD pattern (Figure 1l) were also characterized to reveal the crystallinity of the PdAgCu HMSs, both of which displayed a single set of the peaks assignable to the (111), (200), (220), (311) plane, respectively. Especially, XRD diffraction peaks of PdAgCu HMSs were located in between those of fcc Pd (JCPDS No. 46-1043), fcc Ag (JCPDS No. 04-0783), and fcc Cu (JCPDS No. 04-0836), confirming the formation of trimetallic PdAgCu nanoalloys. We further used the STEM mapping to distinguish chemical compositions and alloyed nanostructures of trimetallic PdAgCu HMSs (Figure 1h). Homogeneous distribution of Pd, Ag, and Cu throughout the whole HMS shell without observable composition segregation indicated the typical solid alloy phase of trimetallic PdAgCu HMSs. The successful formation of HMSs with interior hollow cavity and alloyed PdAgCu composition was also confirmed by STEM line scan (Figure 1i). The composition of Pd, Ag, and Cu in the HMSs was determined to be 54.1:36.4:9.5, in accordance with the result from a X-ray photoelectron spectroscopy (XPS) survey (Figure S2). High-resolution XPS was further fitted to identify the surface electron states (Figure S3). Obviously, the formation of trimetallic PdAgCu nanoalloy gave rise to a positive shift in binding energy than their monometallic counterparts, indicating the upshift of core levels in the Fermi level.[41−43] Slightly oxidized species (Pd^{2+}, Ag^+, and Cu^{2+}) by peak deconvolution further implied the formation of trimetallic PdAgCu nanoalloys.

The above morphological and structural characterizations correlated that trimetallic PdAgCu HMSs were composed of highly uniform nanostructures and chemical compositions with a well-defined interior hollow cavity and cylindrically opened mesoporous shell. We reasoned that "dual" templates of rod and vesicle micelles assembled by the surfactant of DODAC as well as appropriate metal precursors cooperatively facilitated the formation of trimetallic PdAgCu HMSs. First, amphiphilic surfactant of DODAC with two hydrophobic tails and one

DOI: 10.1021/acscentsci.8b00490
ACS Cent. Sci. 2018, 4, 1412−1419

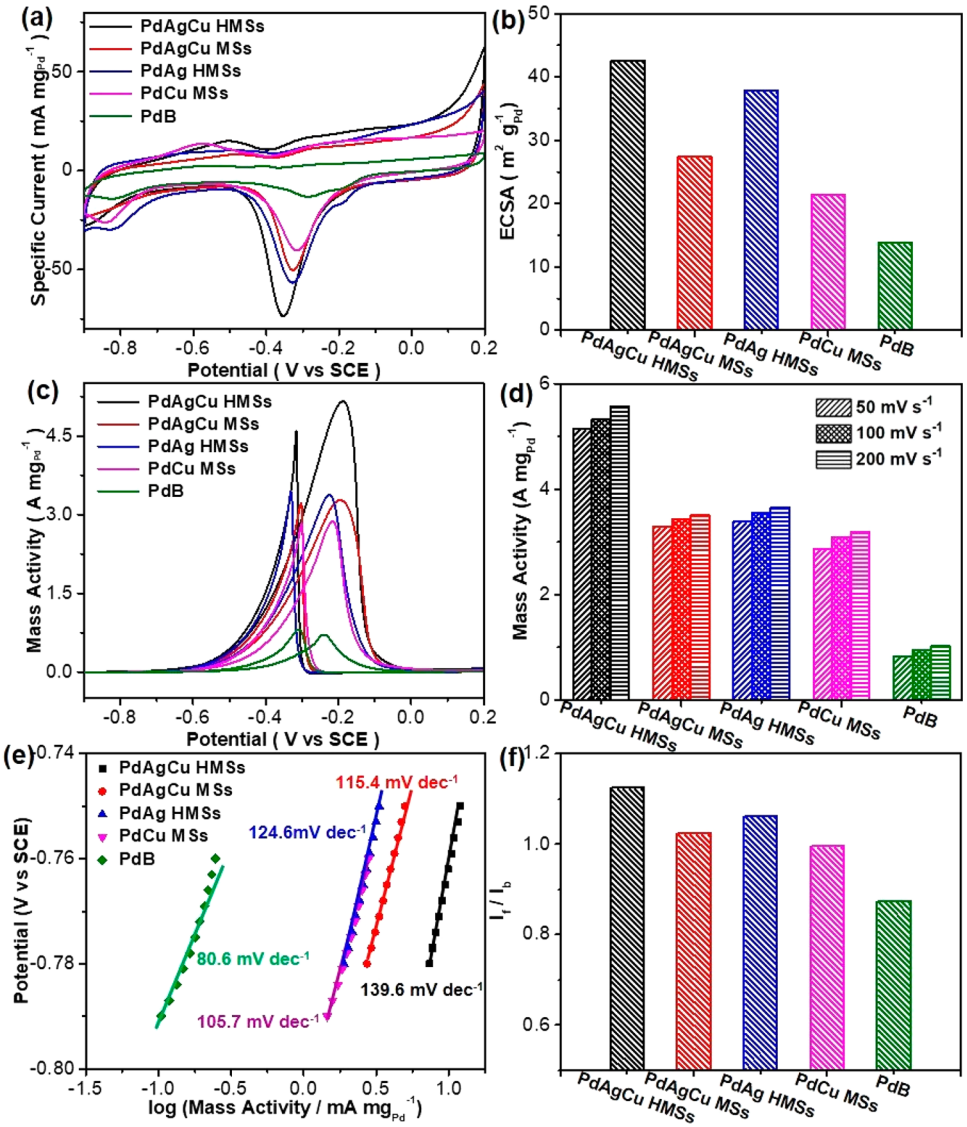

Figure 3. Electrochemical EOR performances. (a) CV curves and (b) summarized ECSAs of trimetallic PdAgCu HMSs and MSs, bimetallic PdAg HMSs and PdCu MSs and commercial PdB obtained in 1.0 M KOH with a scan rate of 50 mV s^{-1}. (c) CV curves, (d) summarized mass activities, (e) Tafel plots, and (f) I_f/I_b values of PdAgCu HMSs and MSs, PdAg HMSs, PdCu MSs, and PdB collected in 1.0 M KOH and 1.0 M ethanol with a scan rate of 50 mV s^{-1}.

hydrophilic quaternary head (see chemical structure in Figure S4) self-assembled into rod and vesicle "dual" micelle structures simultaneously in an aqueous solution at the low temperature of 25 °C and low critical aggregation concentration (cac) of 0.5 mM.[44,45] Similar observations were also achieved by the surfactants of (−)-*N*-dodecyl-*N*-methylephedrinium bromide,[10] and mixed surfactants of *N*-stearoyl-L-glutamic acid and Brij-56 ($C_{16}H_{31}$-$(OCH_2CH_2)_{10}OH$).[11] Subsequently, the electrostatic interaction between metal precursors and "dual"-template structural directing micelles further facilitated the cooperative assembly into a hollow mesoporous nanostructure and in situ growth of trimetallic PdAgCu nanocrystals along "dual"-template micelles into the HMSs kinetically (Figure 2a). We emphasized that both synthesis conditions (surfactant, reaction temperature, and pH) and metal coprecursors played the critical roles in the formation of HMSs. To confirm our hypothesis and to gain more insights into the formation mechanism of trimetallic PdAgCu HMSs, a series of control experiments were carefully carried out as follows.

First, we explored the effect of metal precursors and found that Ag was vital in the formation of Pd-based HMSs. As shown in Figure 2b,c, only the mesoporous nanosphere (MS) structure was formed for monometallic Pd and bimetallic PdCu nanocrystals, indicating that in situ growth along the rod micelle suppressed along the vesical one in the absence of Ag precursor. By contrast, bimetallic PdAg HMSs were achieved when using Pd and Ag as coprecursors (Figure 2d, see wide-angle XRD in Figure S5). We further investigated the effect of Ag precursor in the formation of trimetallic PdAgCu HMSs by carefully tuning the Ag content (Figure 2e−g; see more TEM images in Figure S6). With a Ag content of 18.7 wt %, the interior hollow cavity appeared (Figure 2e), although MSs still were the major structure as observed in bimetallic PdCu MSs. Increasing the Ag content to >36.4 wt % resulted in the formation of perfect and uniform HMSs (Figure 1 and Figure 2f (52.8 wt %)), indicating the key effect of the Ag precursor. However, with the higher Ag content of 75.0 wt %, the mesoporous shell of HMSs became unclear with the thicker mesoporous wall of 5−10 nm (Figure

DOI: 10.1021/acscentsci.8b00490
ACS Cent. Sci. 2018, 4, 1412−1419

2g). Only irregular nanoparticles were obtained with the higher Ag content (>83.4 wt %), indicating the complete destruction of "dual" template micelles (Figure S6p−r). Similar Ag-directed formation of HMS with interior hollow cavity was also observed in bimetallic PdAg nanoalloys (Figure S7). Ag^+ is easier to be reduced into nanocrystals due to the higher reduction potential of Ag^+/Ag, compared to Pd^{2+}/Pd and Cu^{2+}/Cu.[46,47] Our experimental observations implied that the quicker nucleation rate kinetically accelerated the growth of Pd-based nanocrystals into HMSs along vesicle and rod "dual"-template micelles simultaneously. By contrast, in the slower nucleation rate, thermodynamically stable rod micelles suppressed the vesicle one and resulted in the formation of solid MSs.

Second, the surfactants and synthesis conditions were controlled to further reveal the formation mechanism of HMSs. On the one hand, we found that the cationic surfactants with one hydrophobic tail (cetyltrimethylammonium chloride (C_{16}TAC) and octadecyltrimethylammonium chloride (C_{18}TAC)), anionic surfactant of *N*-(2-carboxyethyl)-*N*,*N*-dimethyloctadecan-1-ammonium chloride (C_{18}TAOC),[48] and nonionic surfactant (Pluronic F127)[39] resulted in the formation of solid PdAgCu MSs, rather than HMSs (Figure S8). These results indicated the importance of DODAC as the "dual"-template structural directing surfactant in the formation of the HMSs. On the other hand, the self-assembled micelle nanostructures of DODAC are strongly sensitive to the reaction conditions.[44,45,49] The pH of the reaction solution was first investigated by the addition of HCl and NaOH, and corresponding results are summarized in Figure 2h−j (see Figure S9 for more TEM images). Initially solid MS structures in the lower pH of 2.0 (Figure 2h) gradually evolved into HMS ones with a small interior hollow cavity (<30 nm) with increasing pH to be 3.3 (Figure 2i). The interior hollow cavity became bigger and clearer, and the mesoporous shell was also thinner and uniform in the pH of 6.4 (Figure 1). At a higher pH of 11.8, interestingly, only hollow nanospheres with the solid shell (not mesoporous) were obtained (Figure 2j). The different pH would intrinsically change the packing parameter (*g* value) of the surfactants (DODAC), and thus alter the assembled micelle nanostructures.[44,45,48,50,51] The results indicated that the micelle structures of DODAC changed from rod, to "dual" rod and vesicle, finally to pure vesicle with the increase of pH of the reaction solution. The results definitely verified the existence of "dual"-template structure directing micelles during the synthesis of the HMSs. The effect on "dual" templates of DODAC was also discussed by changing reaction temperatures (Figure S10). Corresponding structural evolution of PdAgCu nanocrystals further indicated the importance of the optimized synthesis conditions for the HMSs.

The above control experiments definitely confirmed that the formation of trimetallic PdAgCu HMSs originated from precise control over crystalline nucleation kinetics and "dual"-template structural directing micelles by the synthesis parameters, including the species of surfactants and metal precursors, and reaction conditions. As far as we know, this work represents the first successful synthesis of hierarchically multimetallic alloyed HMSs with a controlled interior hollow cavity and cylindrically opened mesoporous shell. Trimetallic PdAgCu HMSs combined multiple structural and compositional merits, and thus endowed them with high utilization efficiency of noble metal (Pd), abundant active sites, enlarged surface area, and mass transfer ability, and eventually enhanced electrocatalytic kinetics. Therefore, the HMSs could be employed as highly efficient nanocatalysts with a synergic enhancement effect in EOR for fuel cell applications, with respect to its 0D solid MS and monometallic/bimetallic counterpart nanocatalysts.

The catalytic performance of trimetallic PdAgCu HMSs was evaluated for electrocatalytic EOR in alkaline solution, and the results were compared with those of trimetallic PdAgCu MSs (synthesized with C_{18}TAC as the template, Figure S8d−f), bimetallic PdAg HMSs (Figure 2d), bimetallic PdCu MSs (Figure 2c), and commercial Pd black (PdB) catalysts. Before the electrocatalytic measurements, the catalysts were first washed with acetic acid and modified on glassy carbon electrodes for further electrochemical clean to thoroughly remove the surfactants within the HMSs and MSs (see experimental for more details).[52] Figure 3a shows the cyclic voltammograms (CVs, normalized to the amount of Pd) of the catalysts collected in N_2-saturated 1.0 M KOH with a scan rate of 50 mV s^{-1}. The pronounced cathode signals in the range of −0.6 V and −0.1 V (vs SCE) for all catalysts were seen during the negative sweep, corresponding to the reduction of PdO to Pd.[36,53] Among them, trimetallic PdAgCu HMSs exhibited the lowest reduction peak potential and the largest peak area. This may be responsible for the more accessible active sites and easier PdO reduction ability, and enhanced activity. Electrochemical active surface areas (ECSAs) estimated in the area of PdO reduction peak from CVs[36,43,53,54] were 42.6 m^2 g_{Pd}^{-1} for PdAgCu HMSs, 27.4 m^2 g_{Pd}^{-1} for PdAgCu MSs, 37.9 m^2 g_{Pd}^{-1} for PdAg HMSs, 21.4 m^2 g_{Pd}^{-1} for PdCu MSs, and 13.9 m^2 g_{Pd}^{-1} for commercial PdB, respectively (Figure 3b). The highest ECSA of trimetallic PdAgCu HMSs, which was almost 2 times than that of its MS counterparts and 1.1 times than that of bimetallic counterparts, highlighted synergistically structural and compositional advantages.

Figure 3c shows the CV curves of above five nanocatalysts in the presence of 1 M ethanol, in which the characteristic EOR peaks were clearly identified in both forward and backward scans. It was easy to note that the electrocatalytic activity of EOR strongly corresponded to nanostructures and chemical compositions of the nanocatalysts. Mass peak current density of PdAgCu HMSs, PdAgCu MSs, PdAg HMSs, PdCu MSs, and PdB was 5.13, 3.28, 3.38, 2.87, and 0.83 A mg_{Pd}^{-1}, respectively, at a scan rate of 50 mV s^{-1} (Figure 3d). Obviously, trimetallic PdAgCu HMSs hold the highest EOR mass activity, which was 1.52 times higher than bimetallic counterpart, and 1.56−1.79 times higher than MS counterpart, and 6.18 times higher than commercial PdB catalyst. Meanwhile, the trimetallic PdAgCu HMS is one of the best active EOR electrocatalysts, comparable to these reported nanocatalysts in the literature (Table S1). We further performed the CV scans at different scan rates (10−200 mV s^{-1}) in 1.0 M KOH and 1.0 M ethanol (Figures S11−S15). A similar mass activity tendency of the catalysts was seen. We also summarized the corresponding relationship between the forward peak current and square root of scan rate ($v^{1/2}$). A well-matched linear relationship indicated a diffusion-controlled process during the EOR electrocatalysis for the nanocatalysts.[54] Lastly, the electrocatalytic stability of the catalysts was evaluated by current−time (i−t) chronoamperometry measurements at a potential of −0.2 V (Figure S16). A fast activity loss was found for commercial PdB catalyst after the electrocatalysis for 2000 s. On the contrary, a slightly slower loss in activity was achieved for bimetallic and trimetallic HMSs and MSs. Specially, trimetallic PdAgCu HMSs retained a mass activity of 1.09 A mg_{pd}^{-1} after the electrocatalysis, which was 18.2 times higher than that of PdB (0.06 A mg_{pd}^{-1}). The enhanced stability can be ascribed to 3D

DOI: 10.1021/acscentsci.8b00490
ACS Cent. Sci. 2018, 4, 1412−1419

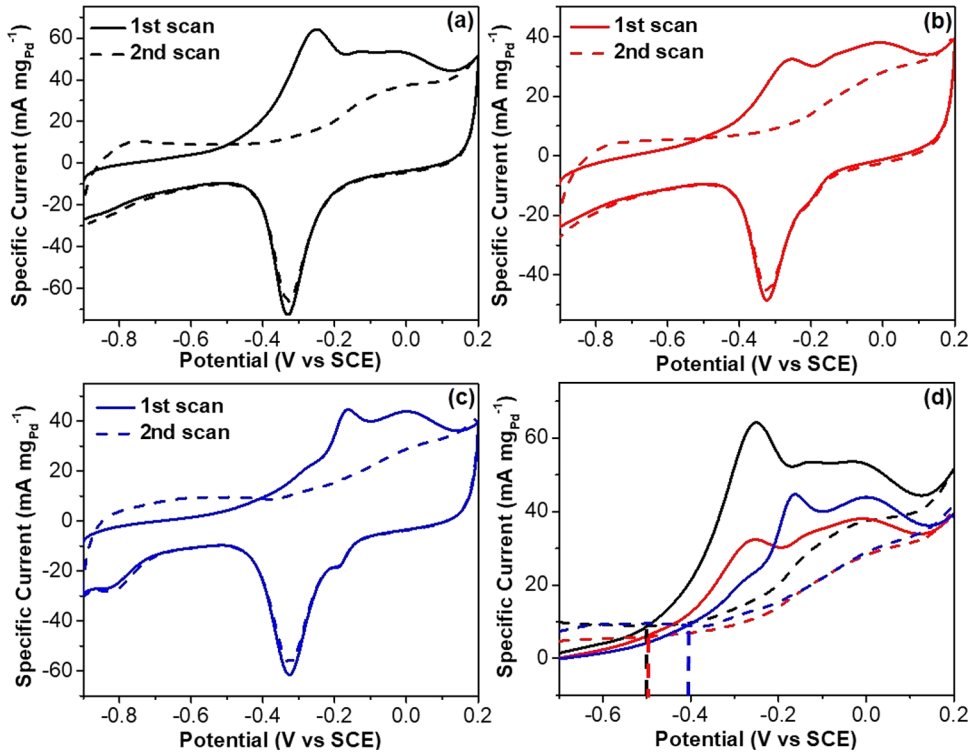

Figure 4. CO antipoisoning experiments. CO stripping voltammograms for (a) trimetallic PdAgCu HMSs, (b) trimetallic PdAgCu MSs, and (c) bimetallic PdAg HMSs in 1.0 M KOH at a scan rate of 50 mV s^{-1}. (d) Overlap of CVs shown in (a−c) recorded in the potential range of −0.7 and 0.2 V.

hollow mesoporous nanostructures that enhanced the contraction affinity with carbon support and greatly facilitated the electron and mass transfer during the electrocatalysis, and thus suppressed the dissolution and Ostwald ripening of PdAgCu HMSs.[55,56]

Electrocatalytic kinetics was also revealed by direct observations on Tafel plots and the ratios of the forward peak current (I_f) to the backward peak current (I_b) (I_f/I_b). As shown in Figure 3e, Tafel plots, which behaved in the current region of −0.8 and −0.7 V,were also responsible for the nanostructures and elemental compositions of the catalysts strongly. Both the larger Tafel plot (140 mV dec^{-1}) and highest output current (−0.78 to —0.75 V) were seen for trimetallic PdAgCu HMSs, identifying the faster electrochemical kinetics during the EOR electrocatalysis.[54,57] Meanwhile, the highest I_f/I_b value of 1.125 indicated PdAgCu HMSs possessed a better tolerance to carbonaceous (CH_3CO and CO) intermediates (Figure 3f).[54] These results further implied that both trimetallic PdAgCu compositions and hollow mesoporous nanostructures contributed synergistically to enhanced electrocatalytic kinetics, and thus boosted EOR performance.

In alkaline media, electrocatalytic EOR generally proceeds on metal (M) catalysts via the following multiple pathways:[36,53,58]

$$M + CH_3CH_2OH + 3OH^- \rightarrow M\text{-}(CH_3CO)_{ads} + 3H_2O + 3e^- \quad \text{fast} \quad (1)$$

$$M + OH^- \rightarrow M\text{-}OH_{ads} + e^- \quad \text{fast} \quad (2)$$

$$M\text{-}(CH_3CO)_{ads} + M\text{-}OH_{ads} \rightarrow M\text{-}CH_3COOH + M \quad \text{slow} \quad (3)$$

$$M\text{-}CH_3COOH + OH^- \rightarrow M + CH_3COO^- + H_2O \quad \text{fast} \quad (4)$$

During the electrocatalysis, the adsorbed poisoning carbonaceous intermediate of CH_3CO on M surface ($M\text{-}(CH_3CO)_{ads}$) as well as its decomposed intermediates of $M\text{-}CO_{ads}$ and $M\text{-}(CH_3)_{ads}$ would block the active sites and thus inactivate nanocatalysts. Introduction of sufficiently adsorbed OH ($M\text{−}OH_{ads}$) intrinsically facilitates the reaction between $M\text{-}(CH_3CO)_{ads}$ and $M\text{−}OH_{ads}$ directly (the rate-determining step, eq 3), and thus accelerates the oxidation and/or removal of $M\text{-}(CH_3CO)_{ads}$ and eventually enhances the electrocatalytic EOR performance.[36,53] Trimetallic PdAgCu HMSs combine synergetic advantages to boost the electrocatalytic kinetics and thus enhance EOR performance. On the one hand, oxophilic Ag and Cu sites can compositionally facilitate the adsorption of OH_{ads} by $Ag\text{−}OH_{ads}$ and $Cu\text{−}OH_{ads}$, and kinetically accelerate eq 3. Meanwhile, alloyed Ag and Cu in Pd would modify the electron structure of Pd (as indicated by XPS) and thus weaken the adsorption and affinity of $(CH_3CO)_{ads}$ on Pd, compared to monometallic Pd and bimetallic PdAg counterparts.[43] This also results in the easier removal of $Pd\text{-}(CH_3CO)_{ads}$ and enhanced activity. On the other hand, hollow mesostructured nanospheres with cylindrically opened nanochannels of the HMSs structurally possess more accessible active sites and easier mass transfer ability (both reactants, intermediates, and products). This also causes the enhanced electrocatalytic kinetics for EOR.

The better desorption kinetics of adsorbed poisoning carbonaceous intermediates on trimetallic PdAgCu HMSs was also identified by CO stripping tests (Figure 4). Two consecutive CV curves of trimetallic PdAgCu HMSs and MSs, and bimetallic PdAg HMSs were recorded in the range of −0.9 and 0.2 V at a scan rate of 50 mV s^{-1}. Complete elimination of CO_{ads} was observed after the second forward scan (Figure 4a−c), indicating the better CO antipoisoning ability of those catalysts. We further compared the onset potentials and active areas of CO oxidation peak by overlapping the CVs. As marked in Figure 4d, trimetallic

DOI: 10.1021/acscentsci.8b00490
ACS Cent. Sci. 2018, 4, 1412−1419

PdAgCu HMSs and MSs showed a similar onset potential at −0.50 V, 0.09 V negatively than that of bimetallic PdAg HMSs. Furthermore, trimetallic PdAgCu HMSs possessed the largest active area of the oxidation peak, which was ∼1.5 times higher than PdAgCu MSs or PdAg HMSs. Both more negative onset potential and larger surface area of CO oxidation peak indicated the enhanced CO oxidation/removal activity and better CO antipoisoning behavior kinetically.[36,53] These results further confirmed synergistically compositional and structural advantages of trimetallic PdAgCu HMSs for electrocatalytic EOR as discussed above.

CONCLUSION

In conclusion, we reported, for the first time, a "dual"-template-directed synthesis method to grow in situ well-dispersed and uniform multimetallic nanoalloyed HMSs in an aqueous solution. The HMSs featured multimetallic (PdAg-based) composition and hollow mesoporous nanostructure with controlled interior hollow cavity and cylindrically opened mesoporous shell. Control experiments confirmed that the optimal synthesis parameters, including metal precursors, surfactants, and reaction conditions, should be seriously considered for the formation of multimetallic HMSs. Compositional and structural advantages of trimetallic PdAgCu HMSs synergistically boosted the electrocatalytic performance for EOR in alkaline solution by kinetically improving the formation of OH_{ads} and facilitating the removal of $(CH_3CO)_{ads}$ and its decomposed intermediates. Our synthesis strategy on the "dual"-template route can be readily extended to other multimetallic nanoalloyed HMSs with desired functions and provide a new avenue to design high-performance nanocatalysts with a synergistic enhancement effect. Trimetallic PdAgAu HMSs and tetrametallic PdAgAuCu HMSs were successfully formed by the "dual"-template method as examples (Figure S17).

ASSOCIATED CONTENT

Supporting Information

The Supporting Information is available free of charge on the ACS Publications website at DOI: 10.1021/acscentsci.8b00490.

Details on synthesis, electrochemical measurements and structural characterizations as well as additional TEM images and electrocatalytic EOR performances (PDF)

AUTHOR INFORMATION

Corresponding Authors

*(D.X.) E-mail: ddxu@njnu.edu.cn.
*(B.L.) E-mail: ben.liu@njnu.edu.cn.

ORCID

Dongdong Xu: 0000-0003-1403-8088
Ben Liu: 0000-0003-1305-5900

Notes

The authors declare no competing financial interest.

ACKNOWLEDGMENTS

The authors thank the financial support from Jiangsu Specially Appointed Professor Plan, National Natural Science Foundation of China (No. 21501095), and Natural Science Foundation of Jiangsu Province (No. BK20150969). This work is also supported by Priority Academic Program Development of Jiangsu Higher Education Institutions, National and Local Joint Engineering Research Center of Biomedical Functional Materials.

REFERENCES

(1) Jain, P. K.; Huang, X.; El-Sayed, I. H.; El-Sayed, M. A. Noble metals on the nanoscale: optical and photothermal properties and some applications in imaging, sensing, biology, and medicine. *Acc. Chem. Res.* **2008**, *41*, 1578−1586.

(2) Bianchini, C.; Shen, P. K. Palladium-based electrocatalysts for alcohol oxidation in half cells and in direct alcohol fuel cells. *Chem. Rev.* **2009**, *109*, 4183−4206.

(3) Yang, K.; Liu, Y.; Liu, Y.; Zhang, Q.; Kong, C.; Yi, C.; Zhou, Z.; Wang, Z.; Zhang, G.; Zhang, Y.; Khashab, N. M.; Chen, X.; Nie, Z. Cooperative assembly of magneto-nanovesicles with tunable wall thickness and permeability for MRI-guided drug delivery. *J. Am. Chem. Soc.* **2018**, *140*, 4666−4677.

(4) Green, I. X.; Tang, W.; Neurock, M.; Yates, J. T. Spectroscopic observation of dual catalytic sites during oxidation of CO on a Au/TiO_2 catalyst. *Science* **2011**, *333*, 736−739.

(5) Li, Y.; Shi, J. Hollow-structured mesoporous materials: chemical synthesis, functionalization and applications. *Adv. Mater.* **2014**, *26*, 3176−3205.

(6) Wang, X.; Feng, J.; Bai, Y.; Zhang, Q.; Yin, Y. Synthesis, properties, and applications of hollow micro-/nanostructures. *Chem. Rev.* **2016**, *116*, 10983−11060.

(7) Yu, L.; Hu, H.; Wu, H. B.; Lou, X. W. Complex hollow nanostructures: synthesis and energy-related applications. *Adv. Mater.* **2017**, *29*, 1604563.

(8) Djojoputro, H.; Zhou, X.; Qiao, S.; Wang, L.; Yu, C.; Lu, G. Periodic mesoporous organosilica hollow spheres with tunable wall thickness. *J. Am. Chem. Soc.* **2006**, *128*, 6320−6321.

(9) Fang, X.; Zhao, X.; Fang, W.; Chen, C.; Zheng, N. Self-templating synthesis of hollow mesoporous silica and their applications in catalysis and drug delivery. *Nanoscale* **2013**, *5*, 2205−2218.

(10) Feng, Z.; Li, Y.; Niu, D.; Li, L.; Zhao, W.; Chen, H.; Li, L.; Gao, J.; Ruan, M.; Shi, J. A facile route to hollow nanospheres of mesoporous silica with tunable size. *Chem. Commun.* **2008**, 2629−2631.

(11) Han, L.; Xiong, P.; Bai, J.; Che, S. Spontaneous formation and characterization of silica mesoporous crystal spheres with reverse multiply twinned polyhedral hollows. *J. Am. Chem. Soc.* **2011**, *133*, 6106−6109.

(12) Niu, D.; Ma, Z.; Li, Y.; Shi, J. Synthesis of core-shell structured dual-mesoporous silica spheres with tunable pore size and controllable shell thickness. *J. Am. Chem. Soc.* **2010**, *132*, 15144−15147.

(13) Li, C.; Sato, T.; Yamauchi, Y. Electrochemical synthesis of one−dimensional mesoporous Pt nanorods using the assembly of surfactant micelles in confined space. *Angew. Chem., Int. Ed.* **2013**, *52*, 8050−8053.

(14) Jiang, B.; Li, C.; Malgras, V.; Imura, M.; Tominaka, S.; Yamauchi, Y. Mesoporous Pt nanospheres with designed pore surface as highly active electrocatalyst. *Chem. Sci.* **2016**, *7*, 1575−1581.

(15) Li, Y.; Shi, J.; Hua, Z.; Chen, H.; Ruan, M.; Yan, D. Hollow spheres of mesoporous aluminosilicate with a three-dimensional pore network and extraordinarily high hydrothermal stability. *Nano Lett.* **2003**, *3*, 609−612.

(16) Wang, J.; Xiao, Q.; Zhou, H.; Sun, P.; Yuan, Z.; Li, B.; Ding, D.; Shi, A. C.; Chen, T. Budded, mesoporous silica hollow spheres: hierarchical structure controlled by kinetic self-assembly. *Adv. Mater.* **2006**, *18*, 3284−3288.

(17) Qi, G.; Wang, Y.; Estevez, L.; Switzer, A. K.; Duan, X.; Yang, X.; Giannelis, E. P. Facile and scalable synthesis of monodispersed spherical capsules with a mesoporous shell. *Chem. Mater.* **2010**, *22*, 2693−2695.

(18) Yoon, S. B.; Sohn, K.; Kim, J. Y.; Shin, C. H.; Yu, J. S.; Hyeon, T. Fabrication of carbon capsules with hollow macroporous core/mesoporous shell structures. *Adv. Mater.* **2002**, *14*, 19−21.

(19) Knossalla, J.; Jalalpoor, D.; Schüth, F. Hands-on guide to the synthesis of mesoporous hollow graphitic spheres and core-shell materials. *Chem. Mater.* **2017**, *29*, 7062−7072.

DOI: 10.1021/acscentsci.8b00490
ACS Cent. Sci. 2018, 4, 1412−1419

(20) Li, Z.; Zhang, J.; Guan, B. Y.; Lou, X. W. Mesoporous carbon@titanium nitride hollowspheres as an efficient SeS_2 host for advanced Li-SeS_2 batteries. *Angew. Chem., Int. Ed.* **2017**, *56*, 16003−16007.
(21) Wang, H.; Jeong, H. Y.; Imura, M.; Wang, L.; Radhakrishnan, L.; Fujita, N.; Castle, T.; Terasaki, O.; Yamauchi, Y. Shape-and size-controlled synthesis in hard templates: sophisticated chemical reduction for mesoporous monocrystalline platinum nanoparticles. *J. Am. Chem. Soc.* **2011**, *133*, 14526−14529.
(22) Prieto, G.; Tüysüz, H.; Duyckaerts, N.; Knossalla, J.; Wang, G.-H.; Schüth, F. Hollow nano-and microstructures as catalysts. *Chem. Rev.* **2016**, *116*, 14056−14119.
(23) Ataee-Esfahani, H.; Liu, J.; Hu, M.; Miyamoto, N.; Tominaka, S.; Wu, K. C.; Yamauchi, Y. Mesoporous metallic cells: design of uniformly sized hollow mesoporous Pt-Ru particles with tunable shell thicknesses. *Small* **2013**, *9*, 1047−1051.
(24) Zhao, M.; Wang, X.; Yang, X.; Gilroy, K. D.; Qin, D.; Xia, Y. Hollow metal nanocrystals with ultrathin, porous walls and well-controlled surface structures. *Adv. Mater.* **2018**, *30*, 1801956.
(25) Zhang, L.; Chang, Q.; Chen, H.; Shao, M. Recent advances in palladium-based electrocatalysts for fuel cell reactions and hydrogen evolution reaction. *Nano Energy* **2016**, *29*, 198−219.
(26) Seh, Z. W.; Kibsgaard, J.; Dickens, C. F.; Chorkendorff, I.; Nørskov, J. K.; Jaramillo, T. F. Combining theory and experiment in electrocatalysis: Insights into materials design. *Science* **2017**, *355*, No. eaad4998.
(27) Luo, M.; Sun, Y.; Wang, L.; Guo, S. Tuning multimetallic ordered intermetallic nanocrystals for efficient energy electrocatalysis. *Adv. Energy Mater.* **2017**, *7*, 1602073.
(28) Liu, H.-l.; Nosheen, F.; Wang, X. Noble metal alloy complex nanostructures: controllable synthesis and their electrochemical property. *Chem. Soc. Rev.* **2015**, *44*, 3056−3078.
(29) Wang, L.; Yamauchi, Y. Strategic synthesis of trimetallic Au@Pd@Pt core-shell nanoparticles from poly (vinylpyrrolidone)-based aqueous solution toward highly active electrocatalysts. *Chem. Mater.* **2011**, *23*, 2457−2465.
(30) Ataee-Esfahani, H.; Wang, L.; Nemoto, Y.; Yamauchi, Y. Synthesis of bimetallic Au@Pt nanoparticles with Au core and nanostructured Pt shell toward highly active electrocatalysts. *Chem. Mater.* **2010**, *22*, 6310−6318.
(31) Shi, Q.; Zhang, P.; Li, Y.; Xia, H.; Wang, D.; Tao, X. Synthesis of open-mouthed, yolk−shell Au@AgPd nanoparticles with access to interior surfaces for enhanced electrocatalysis. *Chem. Sci.* **2015**, *6*, 4350−4357.
(32) Wang, Y.; Wang, G.; Li, G.; Huang, B.; Pan, J.; Liu, Q.; Han, J.; Xiao, L.; Lu, J.; Zhuang, L. Pt-Ru catalyzed hydrogen oxidation in alkaline media: oxophilic effect or electronic effect? *Energy Environ. Sci.* **2015**, *8*, 177−181.
(33) Demirci, U. B. Theoretical means for searching bimetallic alloys as anode electrocatalysts for direct liquid-feed fuel cells. *J. Power Sources* **2007**, *173*, 11−18.
(34) Strasser, P.; Koh, S.; Anniyev, T.; Greeley, J.; More, K.; Yu, C.; Liu, Z.; Kaya, S.; Nordlund, D.; Ogasawara, H.; Toney, M. F.; Nilsson, A. Lattice-strain control of the activity in dealloyed core-shell fuel cell catalysts. *Nat. Chem.* **2010**, *2*, 454.
(35) Mahmood, A.; Xie, N.; Din, M. A. U.; Saleem, F.; Lin, H.; Wang, X. Shape controlled synthesis of porous tetrametallic PtAgBiCo nanoplates as highly active and methanol-tolerant electrocatalyst for oxygen reduction reaction. *Chem. Sci.* **2017**, *8*, 4292−4298.
(36) Hong, J. W.; Kim, Y.; Wi, D. H.; Lee, S.; Lee, S. U.; Lee, Y. W.; Choi, S. I.; Han, S. W. Ultrathin free-standing ternary-alloy nanosheets. *Angew. Chem., Int. Ed.* **2016**, *55*, 2753−2758.
(37) Wang, H.; Luo, W.; Zhu, L.; Zhao, Z.; E, B.; Tu, W.; Ke, X.; Sui, M.; Chen, C.; Chen, Q.; Li, Y.; Huang, Y. Synergistically enhanced oxygen reduction electrocatalysis by subsurface atoms in ternary PdCuNi alloy catalysts. *Adv. Funct. Mater.* **2018**, *28*, 1707219.
(38) Hong, F.; Sun, S.; You, H.; Yang, S.; Fang, J.; Guo, S.; Yang, Z.; Ding, B.; Song, X. Cu_2O template strategy for the synthesis of structure-definable noble metal alloy mesocages. *Cryst. Growth Des.* **2011**, *11*, 3694−3697.
(39) Jiang, B.; Li, C.; Imura, M.; Tang, J.; Yamauchi, Y. Multimetallic mesoporous spheres through surfactant-directed synthesis. *Adv. Sci.* **2015**, *2*, 1500112.
(40) Han, S.-H.; Bai, J.; Liu, H.-M.; Zeng, J.-H.; Jiang, J.-X.; Chen, Y.; Lee, J.-M. One-pot fabrication of hollow and porous Pd-Cu alloy nanospheres and their remarkably improved catalytic performance for hexavalent chromium reduction. *ACS Appl. Mater. Interfaces* **2016**, *8*, 30948−30955.
(41) Fu, S.; Zhu, C.; Du, D.; Lin, Y. Facile one-step synthesis of three-dimensional Pd-Ag bimetallic alloy networks and their electrocatalytic activity toward ethanol oxidation. *ACS Appl. Mater. Interfaces* **2015**, *7*, 13842−13848.
(42) Han, S. H.; Liu, H. M.; Chen, P.; Jiang, J. X.; Chen, Y. Porous trimetallic PtRhCu cubic nanoboxes for ethanol electrooxidation. *Adv. Energy Mater.* **2018**, *8*, 1801326.
(43) Huang, W.; Kang, X.; Xu, C.; Zhou, J.; Deng, J.; Li, Y.; Cheng, S. 2D PdAg alloy nanodendrites for enhanced ethanol electroxidation. *Adv. Mater.* **2018**, *30*, 1706962.
(44) Feitosa, E.; Barreleiro, P.; Olofsson, G. Phase transition in dioctadecyldimethylammonium bromide and chloride vesicles prepared by different methods. *Chem. Phys. Lipids* **2000**, *105*, 201−213.
(45) Laughlin, R.; Munyon, R.; Fu, Y.; Fehl, A. Physical science of the dioctadecyldimethylammonium chloride-water system. 1. Equilibrium phase behavior. *J. Phys. Chem.* **1990**, *94*, 2546−2552.
(46) Wiley, B.; Sun, Y.; Mayers, B.; Xia, Y. Shape-controlled synthesis of metal nanostructures: the case of silver. *Chem. - Eur. J.* **2005**, *11*, 454−463.
(47) Liu, B.; Jin, L.; Zhong, W.; Lopes, A.; Suib, S. L.; He, J. Ultrafine and ligand-free precious metal (Ru, Ag, Au, Rh and Pd) nanoclusters supported on phosphorus-doped carbon. *Chem. - Eur. J.* **2018**, *24*, 2565−2569.
(48) Xu, D.; Liu, X.; Lv, H.; Liu, Y.; Zhao, S.; Han, M.; Bao, J.; He, J.; Liu, B. Ultrathin palladium nanosheets with selectively controlled surface facets. *Chem. Sci.* **2018**, *9*, 4451−4455.
(49) Bakshi, M. S. How surfactants control crystal growth of nanomaterials. *Cryst. Growth Des.* **2016**, *16*, 1104−1133.
(50) Xu, D.; Liu, X.; Han, M.; Bao, J. Facile synthesis of ultrathin single-crystalline palladium nanowires with enhanced electrocatalytic activities. *Chem. Commun.* **2016**, *52*, 12996−12999.
(51) Nagarajan, R. Molecular packing parameter and surfactant self-assembly: the neglected role of the surfactant tail. *Langmuir* **2002**, *18*, 31−38.
(52) Yang, H.; Tang, Y.; Zou, S. Electrochemical removal of surfactants from Pt nanocubes. *Electrochem. Commun.* **2014**, *38*, 134−137.
(53) Chen, L.; Lu, L.; Zhu, H.; Chen, Y.; Huang, Y.; Li, Y.; Wang, L. Improved ethanol electrooxidation performance by shortening Pd-Ni active site distance in Pd-Ni-P nanocatalysts. *Nat. Commun.* **2017**, *8*, 14136.
(54) Yang, Y.; Jin, L.; Liu, B.; Kerns, P.; He, J. Direct growth of ultrasmall bimetallic AuPd nanoparticles supported on nitrided carbon towards ethanol electrooxidation. *Electrochim. Acta* **2018**, *269*, 441−451.
(55) Wang, L.; Yamauchi, Y. Metallic nanocages: synthesis of bimetallic Pt-Pd hollow nanoparticles with dendritic shells by selective chemical etching. *J. Am. Chem. Soc.* **2013**, *135*, 16762−16765.
(56) Wang, M.; Zhang, W.; Wang, J.; Minett, A.; Lo, V.; Liu, H.; Chen, J. Mesoporous hollow PtCu nanoparticles for electrocatalytic oxygen reduction reaction. *J. Mater. Chem. A* **2013**, *1*, 2391−2394.
(57) Liang, Z.; Zhao, T.; Xu, J.; Zhu, L. Mechanism study of the ethanol oxidation reaction on palladium in alkaline media. *Electrochim. Acta* **2009**, *54*, 2203−2208.
(58) Christensen, P.; Jones, S.; Hamnett, A. An *in situ* FTIR spectroscopic study of the electrochemical oxidation of ethanol at a Pb-modified polycrystalline Pt electrode immersed in aqueous KOH. *Phys. Chem. Chem. Phys.* **2013**, *15*, 17268−17276.

DOI: 10.1021/acscentsci.8b00490
ACS Cent. Sci. 2018, 4, 1412−1419